DUST GENERATION MECHANISMS AND EFFECTS OF OPERATING PARAMETERS IN A FLAIL-TYPE STRAW PICKUP HEADER USING DEM AND CFD
/
基于 DEM 与 CFD 的锤爪式秸秆捡拾割台扬尘机理与作业参数影响

Jinghao FAN[1,2], Haiqing TIAN*[1,2], Chunxiang ZHUO[1,2], Kai ZHAO[1,2], Qiang YUE[1,2], Ruiyi XU[1,2]
[1] College of Mechanical and Electrical Engineering, Inner Mongolia Agricultural University, Hohhot 010018, China.
[2] Inner Mongolia Engineering Research Centre of Intelligent Equipment for the Entire Process of Forage and Feed Production, Hohhot 010018, China.
Tel: 15947019846; E-mail: hqtian@126.com
DOI: https://doi.org/10.35633/inmateh-79-102

Keywords: *flail-type pickup header; dust generation; discrete element method; computational fluid dynamics; particulate matter*

ABSTRACT
Airborne dust generated during straw pickup can impair operating visibility and local air quality; however, the respective contributions of mechanical particle detachment and aerodynamic entrainment in flail-type pickup headers remain insufficiently quantified. This study combined discrete element method (DEM) and computational fluid dynamics (CFD) analyses with field measurements to investigate these two processes. A bonded corn root stubble–soil DEM model was established in EDEM, and the bond fracture rate was used to characterize the relative degree of particle detachment. The effects of ground clearance (30–90 mm), rotor speed (4100–5300 rpm), forward speed (0.5–1.5 m/s), plant spacing (200–300 mm), and row spacing (300–500 mm) were evaluated. CFD simulations were then used to characterize the time-averaged airflow field within the pickup-header housing. Increasing the ground clearance from 30 to 90 mm reduced the bond fracture rate by 44.5%, whereas increasing the rotor speed from 4100 to 5300 rpm increased it by 52.3%. By relating the DEM particle-detachment states to the CFD flow-field characteristics, three dust-generation pathways were identified: stubble fragmentation, root extraction, and direct entrainment of loose surface particles. Rotor speed affected both mechanical detachment and airflow entrainment at the header inlet. Field measurements showed that the selected low-dust operating condition, with a ground clearance of 75 mm, rotor speed of 4400 rpm, and forward speed of 0.75 m/s, reduced total suspended particulate (TSP), PM_{10}, and $PM_{2.5}$ concentrations by 62.2%, 58.4%, and 53.8%, respectively, compared with the dust-intensive condition. By linking particle detachment, airflow entrainment, and field measurements within a mechanism-based framework, this study clarifies the effects of operating parameters on dust generation and provides a basis for selecting low-dust operating parameters and improving pickup-header inlet design.

摘要
秸秆捡拾过程中产生的扬尘会降低作业视野并恶化局部空气质量，但锤爪式捡拾割台中机械颗粒脱离与气流卷吸各自对扬尘形成的作用仍缺乏充分的定量认识。本研究将相互独立的离散元法(DEM)分析、计算流体动力学(CFD)分析与田间测试相结合，对上述两类过程进行了研究。利用 EDEM 建立玉米根茬—土壤粘结颗粒模型，并采用粘结键断裂率表征颗粒相对脱离程度，考察离地高度(30-90 mm)、锤爪转速(4100-5300 rpm)、前进速度(0.5-1.5 m/s)、株距(200-300 mm)和行距(300-500 mm)的影响。随后利用 CFD 模拟分析捡拾割台壳体内部的时均气流特征。离地高度由 30 mm 增加至 90 mm 时，粘结键断裂率降低 44.5%；锤爪转速由 4100 rpm 增加至 5300 rpm 时，粘结键断裂率提高 52.3%。通过将 DEM 获得的颗粒脱离状态与 CFD 流场特征对应分析，推断出三条扬尘产生途径：根茬破碎、根茬拔除以及土壤表面松散颗粒的直接气流卷吸。锤爪转速同时影响机械颗粒脱离和入口气流卷吸。田间试验表明，相较于高扬尘工况，离地高度 75 mm、锤爪转速 4400 rpm、前进速度 0.75 m/s 的低尘工况使 TSP、PM_{10} 和 $PM_{2.5}$ 浓度分别降低 62.2%、58.4%和 53.8%。本研究通过在统一的机理框架下关联颗粒脱离、气流卷吸和田间实测结果，阐明了作业参数影响扬尘形成的作用途径，可为低尘作业参数选择及捡拾割台入口结构改进提供依据。

INTRODUCTION
Agricultural field operations can generate substantial airborne particulate matter through the disturbance of soil and crop residues. Total suspended particulate (TSP), particulate matter with an aerodynamic diameter below 10 μm (PM_{10}), and particulate matter below 2.5 μm ($PM_{2.5}$) can deteriorate local air quality and operating conditions, and their emission levels vary with machinery type, soil condition, and operating intensity (*Çarman*

et al., 2023; Chen et al., 2017; Zhang et al., 2023; Chen et al., 2024). Mechanized straw recovery reduces open-field residue burning, but straw pickup itself can generate considerable dust (*Yang et al., 2022*). In a flail-type pickup header, high-speed flails fragment root stubble and detach adhered soil, while rotor-induced negative pressure at the housing inlet entrains detached and loose surface particles. Reported TSP concentrations during harvesting can reach 1500-3000 μg/m^3, and $PM_{2.5}$ may account for 30%-45% of airborne dust (*Zhang et al., 2021; Xu et al., 2022a*). Therefore, source-oriented dust control should address both mechanical detachment and aerodynamic entrainment.

The discrete element method (DEM) has been extensively applied to agricultural machinery–soil interactions. Bonded-particle approaches provide a means of representing cohesive failure and particle separation in granular materials (*Cundall and Strack, 1980; Potyondy and Cundall, 2004*). Agricultural DEM studies have investigated soil–tool interaction, tillage and furrow opening, soil-aggregate fracture, rotary-tillage burial and mixing, and straw–soil–cutting processes (*Zhao et al., 2021; Aikins et al., 2021; Aikins et al., 2023; Du et al., 2022; Foldager et al., 2022; Li et al., 2025*). However, the use of bond failure to characterize particle detachment specifically during high-speed flail interaction with a root stubble–soil composite remains limited.

Computational fluid dynamics (CFD) is well suited to resolving airflow organization and particle-transport conditions within agricultural machinery. Previous studies have applied CFD to optimize airflow distribution in combine-harvester cleaning systems, analyze dust diffusion during harvesting, and evaluate dust-suppression structures (*Liang et al., 2020; Xu et al., 2022b; Xu et al., 2023*). These studies demonstrate that internal airflow plays an important role in dust transport and dispersion. However, existing CFD research has mainly focused on cleaning devices, overall dust diffusion, or suppression structures, while the relationship between the near-ground inlet flow of a flail-type pickup header and the formation of different dust-generation pathways remains insufficiently quantified.

Accordingly, two limitations remain relevant to flail-type straw pickup. First, the mechanical detachment of particles from the root stubble-soil system and their subsequent aerodynamic entrainment have generally been examined as separate processes. Second, the extent to which controllable operating parameters simultaneously affect these two processes has not been clarified through field validation. Therefore, the present study used independent DEM and CFD analyses, rather than a fully coupled DEM-CFD model, and integrated their results with field measurements. The objectives were to: (1) quantify the effects of ground clearance, rotor speed, forward speed, plant spacing, and row spacing on particle detachment; (2) characterize the time-averaged internal flow field and relate its principal regions to potential dust-generation pathways; and (3) evaluate a selected low-dust operating condition using field measurements of TSP, PM_{10}, and $PM_{2.5}$. The main contribution is a mechanism-based framework linking operating parameters to both mechanical detachment and aerodynamic entrainment.

MATERIALS AND METHODS

Structure and Working Principle of the Flail-Type Pickup Header

The flail-type pickup header consists mainly of a flail rotor, housing, mounting frame, transmission system, deflector, and conveying auger (Fig. 1). The main structural parameters are listed in Table 1.

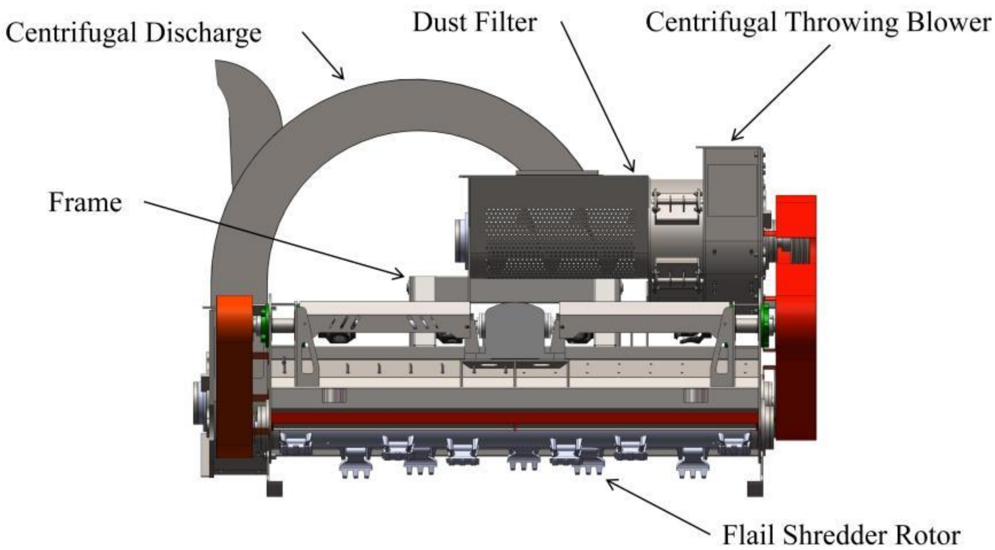

Fig. 1 - Overall Structure

Table 1

Main structural parameters of flail-type pickup header

Parameter	Value
Diameter of flail roller (mm)	180
Length of flail roller (mm)	2200
Number of flails	22
Length of flail (mm)	160

During operation, the rotor turns at 4100-5300 rpm while the machine advances. The flails strike the exposed root stubble without directly contacting the soil surface. Detached material is thrown upward and transported along the housing by the flails and the rotor-induced airflow before entering the conveying auger.

Discrete Element Model of the Root Stubble-Soil Composite

A DEM model of the corn root stubble-soil composite was established in EDEM. Root stubble and 0-100 mm surface-soil samples were obtained from the test field. Material, bonding, and contact parameters were adopted from previously calibrated and validated models for the same material system and operating region (*Zhuo et al., 2025; Xu et al., 2024*).

Table 2

Intrinsic material parameters

Material	Density	Poisson's Ratio	Shear Modulus
	(kg/m³)		(MPa)
Corn Root Stubble	107.5	0.3	6.5
Soil Particles	1646	0.42	4.6
Flail	7850	0.3	79000

The Hertz-Mindlin with Bonding V2 contact model was applied to soil particles and root stubble, as this model can effectively simulate the cohesive forces between moist soil particles (*Potyondy and Cundall, 2004; Aikins et al., 2021*). The bonding parameters are listed in Table 3.

Table 3

Bonding parameters

Contact Pair	Stiffness per Unit Area	Critical Stress	Bonding Radius
	(N/m³)	(MPa)	(mm)
Root-Root	2.2×10^6	2.45	1.38
Soil-Soil	5×10^5	0.31	1.65
Root-Soil	6.5×10^5	0.31	1.38

The contact parameters are listed in Table 4.

Table 4

Contact parameters

Contact Type	Coefficient of Static Friction	Coefficient of Rolling Friction	Coefficient of Restitution
Soil-Soil	0.62	0.1	0.55
Soil-Root Stubble	0.42	0.21	0.6
Soil-Flail	0.60	0.10	0.3
Root Stubble-Flail	0.60	0.10	0.5

The soil bin was generated by natural packing. Root stubble was represented by 2-4 mm bonded spheres, with an approximate diameter of 25 mm and burial depth of 200 mm. Stubble units were arranged according to the prescribed plant and row spacings. The pickup geometry was imported from SolidWorks, and the rotor was assigned simultaneous rotation and forward translation. The time step was 3.6% of the Rayleigh time step.

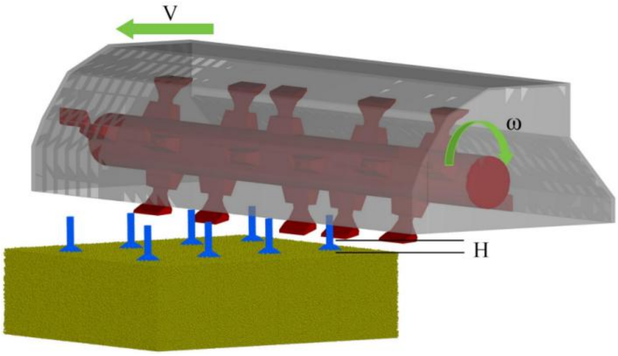

Fig. 2 - Schematic diagram of flail–root stubble interaction

Key Indicators

Because the flails did not directly contact the soil surface, bond failure was used to characterize particle detachment from the stubble-soil matrix. A bond was considered broken when the local stress exceeded its strength limit; the released particles could then be ejected by mechanical impact and subsequently entrained by airflow.

The bond fracture rate η was calculated as the ratio of the number of broken bonds, N_b, to the initial number of bonds, N_0:

$$\eta = \frac{N_b}{N_0} \times 100\% \tag{1}$$

The index was extracted from EDEM post-processing and used to compare the relative degree of particle detachment among operating conditions.

Single-Factor Experiment Design

Five factors were evaluated by single-factor simulations: ground clearance (H), rotor speed (ω), forward speed (v), plant spacing (Δx), and row spacing (Δy). When one factor was varied, the remaining factors were fixed at their intermediate levels (Table 5).

Table 5

Single-factor simulation scheme

Test Number	Operational parameters				
	Ground Clearance	Rotor Speed	Forward Speed	Plant Spacing	Row Spacing
	H **(mm)**	***ω*** **(rpm)**	***v*** **(m/s)**	**Δ*x*** **(mm)**	**Δ*y*** **(mm)**
1	30	4700	1	250	400
2	45	4700	1	250	400
3	60	4700	1	250	400
4	75	4700	1	250	400
5	90	4700	1	250	400
6	60	4100	1	250	400
7	60	4400	1	250	400
8	60	4700	1	250	400
9	60	5000	1	250	400
10	60	5300	1	250	400

Test Number	Operational parameters				
	Ground Clearance	Rotor Speed	Forward Speed	Plant Spacing	Row Spacing
	H (mm)	*ω* (rpm)	*v* (m/s)	Δ*x* (mm)	Δ*y* (mm)
11	60	4700	0.5	250	400
12	60	4700	0.75	250	400
13	60	4700	1	250	400
14	60	4700	1.25	250	400
15	60	4700	1.5	250	400
16	60	4700	1	200	400
17	60	4700	1	225	400
18	60	4700	1	250	400
19	60	4700	1	275	400
20	60	4700	1	300	400
21	60	4700	1	250	300
22	60	4700	1	250	350
23	60	4700	1	250	400
24	60	4700	1	250	450
25	60	4700	1	250	500

In addition to the single-factor simulations, two combined operating conditions were simulated for comparison with the subsequent field measurements. The selected low-dust condition was set at a ground clearance of 75 mm, a rotor speed of 4400 rpm, and a forward speed of 0.75 m/s, whereas the dust-intensive condition was set at 30 mm, 5300 rpm, and 1.0 m/s, respectively. Plant spacing and row spacing were maintained at 250 and 400 mm for both conditions. The DEM model parameters and bond-fracture-rate calculation method were kept consistent with those used in the single-factor simulations.

CFD Model of the Internal Flow Field of the Pickup Header

The internal flow field was modeled in ANSYS Fluent 2020R2. The housing, rotor region, inlet, outlet, and a closed ground boundary were retained, while small features with negligible aerodynamic influence were omitted (Fig. 3).

The computational domain was divided into a rotating rotor region and a stationary housing region connected by an interface. A steady multiple-reference-frame (MRF) model was used to obtain the time-averaged flow field. The MRF approach had previously been validated for the same pickup system by comparing simulated and measured inlet pressure distributions at 35 bench-test points *(Wang et al., 2024b)*.

The mesh contained 14.8 million cells. A pressure-based steady solver, the realizable k-ε turbulence model *(Shih et al., 1995)*, and air as the continuous phase were used. The inlet was specified as a pressure inlet, the conveying channel as the outlet, and the rotor walls moved with the rotating reference frame.

The DEM and CFD simulations were conducted independently and did not constitute a fully coupled DEM-CFD simulation. The DEM analysis was used to characterize the relative degree and spatial features of particle detachment from the root stubble-soil system, whereas the CFD analysis was used to characterize the time-averaged airflow within the pickup-header housing. To relate the two analyses, the locations and modes of particle detachment obtained from DEM were compared with the characteristic airflow regions predicted by CFD. Detachment caused by direct flail impact was examined in relation to the high-speed rotation zone, while disturbance at the root-soil interface was evaluated together with the near-ground inlet flow. In addition, the near-ground inlet velocity was compared with the estimated entrainment thresholds to assess the potential for direct lifting of loose surface particles. Accordingly, the proposed dust-generation pathways were interpreted from complementary mechanical and aerodynamic evidence rather than derived from particle trajectories in a coupled DEM-CFD simulation.

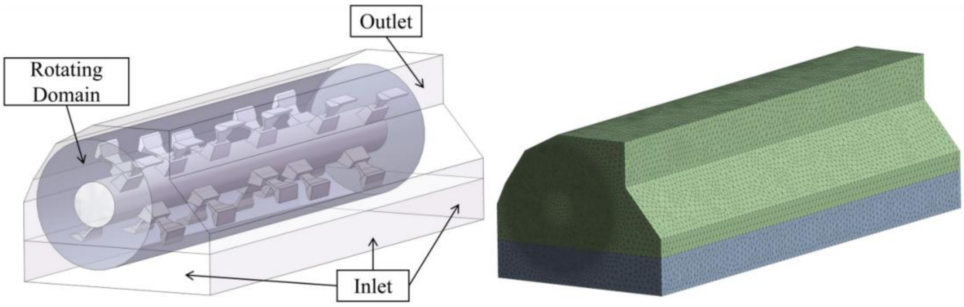

Fig. 3 - Computational Domain and Grid for the Flow Field

Field Experiment

Field tests were conducted in a corn field in Togtoh County, Inner Mongolia, China (40°20′N, 111°30′E; Fig. 4). Measured plant spacing (240-260 mm), row spacing (390-410 mm), and stubble diameter (23-28 mm) were consistent with the DEM settings.

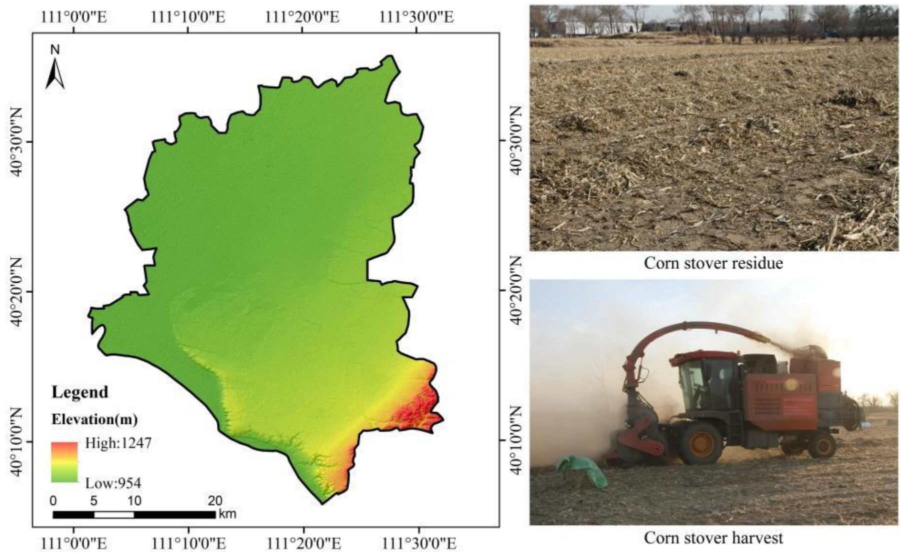

Fig. 4 - Overview of the study area

Two operating conditions were compared using a 4JKZ-240 straw feed baler harvester: a selected low-dust condition (75 mm ground clearance, 4400 rpm rotor speed, and 0.75 m/s forward speed) and a dust-intensive condition (30 mm, 5300 rpm, and 1.0 m/s). The sampling point was located directly above the pickup header (Fig. 5).

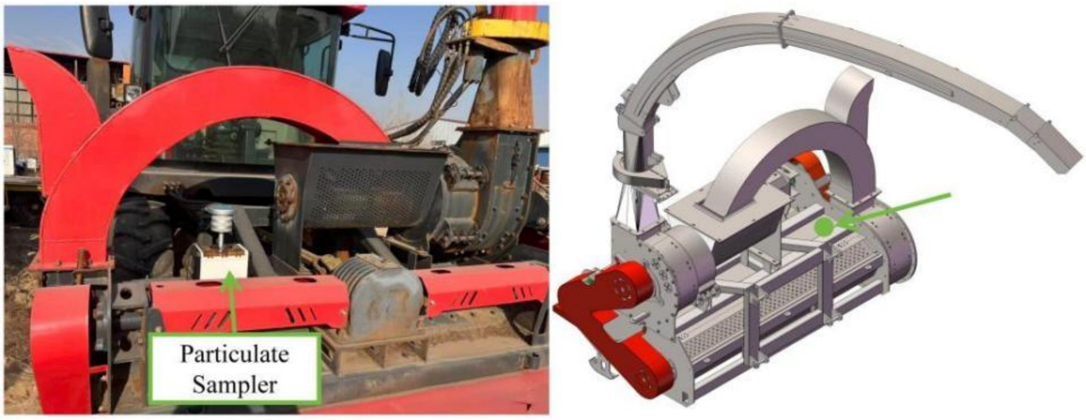

Fig. 5 - Installation Location of the Particulate Sampler

Each operating condition was evaluated in three independent field runs (n = 3). Each replicate consisted of a separate 10-min harvesting pass conducted under the same operating-parameter setting, with particulate sampling performed independently for each run.

The measured concentrations are reported as mean ± standard deviation. TSP was collected on glass-fiber filters with a KB-6120 atmospheric sampler at 100 L/min and determined gravimetrically; size-fractionated samples were collected simultaneously. Filters were conditioned for 24 h at 25 ± 1°C and 50 ± 5% relative humidity before weighing.

$$C = \frac{(m_2 - m_1)}{(Q \times t)} \times 10^6 \tag{2}$$

In Eq. (2), C is the TSP mass concentration (μg/m^3), m_1 and m_2 are the filter masses before and after sampling (g), Q is the sampling flow rate (m^3/min; 0.100 m^3/min in the present experiments), and t is the sampling duration (min). Each replicate was sampled for 10 min.

Statistical comparisons between the two operating conditions were performed using a two-sided Welch's t-test because the measured variability differed between conditions. Statistical significance was evaluated at $p < 0.05$. Given the limited number of field replicates (n = 3 per condition), the statistical results were interpreted together with the observed effect magnitude and descriptive variability.

Aerodynamic Entrainment Threshold Calculation

To evaluate the aerodynamic entrainment potential of soil particles near the pickup-header inlet, the threshold friction velocity was estimated using the simplified relationship proposed by *Shao and Lu (2000)*. The reported wind-speed dependence of agricultural-soil dust flux (*Wang et al., 2021; Wang et al., 2024a*) was further used to estimate the relative change in entrainment intensity among different rotor speeds.

$$u_{*t} = \sqrt{A_N \left[\frac{(\rho_p - \rho_a)}{\rho_a} gd \right]} \tag{3}$$

where u_{*t} is the threshold friction velocity (m/s), A_N is the dimensionless coefficient in the Shao-Lu model, ρ_p and ρ_a are the particle and air densities, respectively, g is gravitational acceleration, and d is the particle diameter. In this study, A_N was set to 0.0123 according to *Shao and Lu (2000)*.

The original Shao-Lu relationship is expressed in terms of friction velocity, whereas the CFD results provide the characteristic mean velocity in the inlet entrainment region. Therefore, the threshold friction velocity was converted into an equivalent mean-flow threshold velocity as follows:

$$U_t = \frac{U}{u_*} u_{*t} = A \sqrt{\left[\frac{(\rho_p - \rho_a)}{\rho_a} gd \right]} \tag{4}$$

where U_t is the equivalent mean-flow threshold velocity, U is the characteristic mean inlet velocity, u_* is the corresponding friction velocity, and A is the effective velocity-conversion coefficient:

$$A = \sqrt{A_N} \frac{U}{u_*} \tag{5}$$

For a first-order engineering estimate, the relationship between the mean velocity and friction velocity was obtained from the Darcy-Weisbach formulation:

$$\frac{U}{u_*} = \sqrt{\frac{8}{f}} \tag{6}$$

where f is the Darcy friction factor. The Blasius correlation for smooth turbulent flow, $f = 0.3164\,\mathrm{Re}^{-0.25}$, was adopted. Based on a characteristic inlet velocity of 5-18 m/s, a hydraulic diameter of approximately 0.2 m, and an air kinematic viscosity of 1.5×10^{-5} m^2/s, the Reynolds number was estimated to be 6.7×10^4-2.4×10^5. The corresponding Darcy friction factor was 0.0143-0.0197, giving $U/u_* \approx 20.2 - 23.7$. Substitution into Eq. (5) yielded an effective coefficient range of 2.24-2.62. A representative intermediate value of $A = 2.43$ was therefore adopted to calculate the equivalent mean-flow threshold velocities of particles with different diameters.

The threshold-exceedance ratio was calculated as the ratio of the upper inlet velocity obtained from CFD to the equivalent mean-flow threshold velocity of each representative particle diameter. The relative entrainment flux among rotor speeds was estimated using the cubic relationship between dust flux and airflow velocity reported in previous studies.

The conversion was introduced to enable a consistent comparison between the threshold friction velocity derived from the Shao-Lu relationship and the characteristic inlet velocity obtained from CFD.

The resulting equivalent mean-flow threshold velocity therefore serves as a comparative criterion for evaluating the aerodynamic entrainment potential of particles under different rotor-speed conditions. The Darcy-Weisbach and Blasius relationships provide the velocity-conversion framework under turbulent-flow conditions, while the actual pickup-header inlet flow remains spatially non-uniform because of rotor-induced rotation and local acceleration. Accordingly, the calculated threshold-exceedance ratio is used to compare relative entrainment intensity among operating conditions rather than to represent an exact local entrainment threshold at every point in the inlet region. Similarly, the cubic relationship between dust flux and airflow velocity is used to estimate the relative change in entrainment intensity rather than the absolute dust mass flux.

RESULTS

Effects of Operating Parameters on Particle Detachment

Under the reference condition of a rotor speed of 4700 rpm, a ground clearance of 60 mm, and a forward speed of 1.0 m/s, the dynamic flail-root stubble interaction was divided into four stages according to the flail position, stubble deformation, and particle detachment state: approach, impact, cutting and fragmentation, and separation and ejection (Fig. 6). Substantial bond breakage occurred during the impact and cutting stages. The detached particles acquired initial velocity from the flail impact and could subsequently be entrained and transported by the airflow inside the housing. The effects of the five operating parameters on bond fracture rate are presented in Figs. 7 and 8.

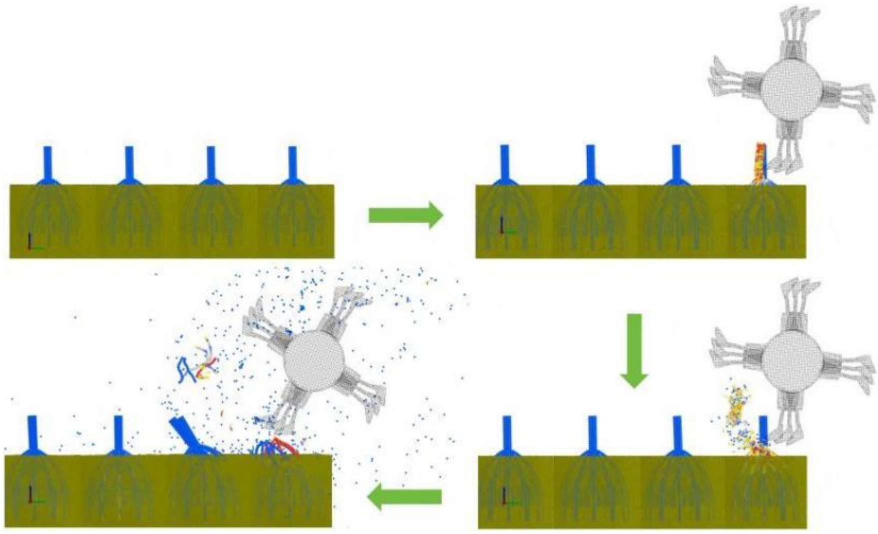

Fig. 6 - Dynamic interaction process between the flail and root stubble

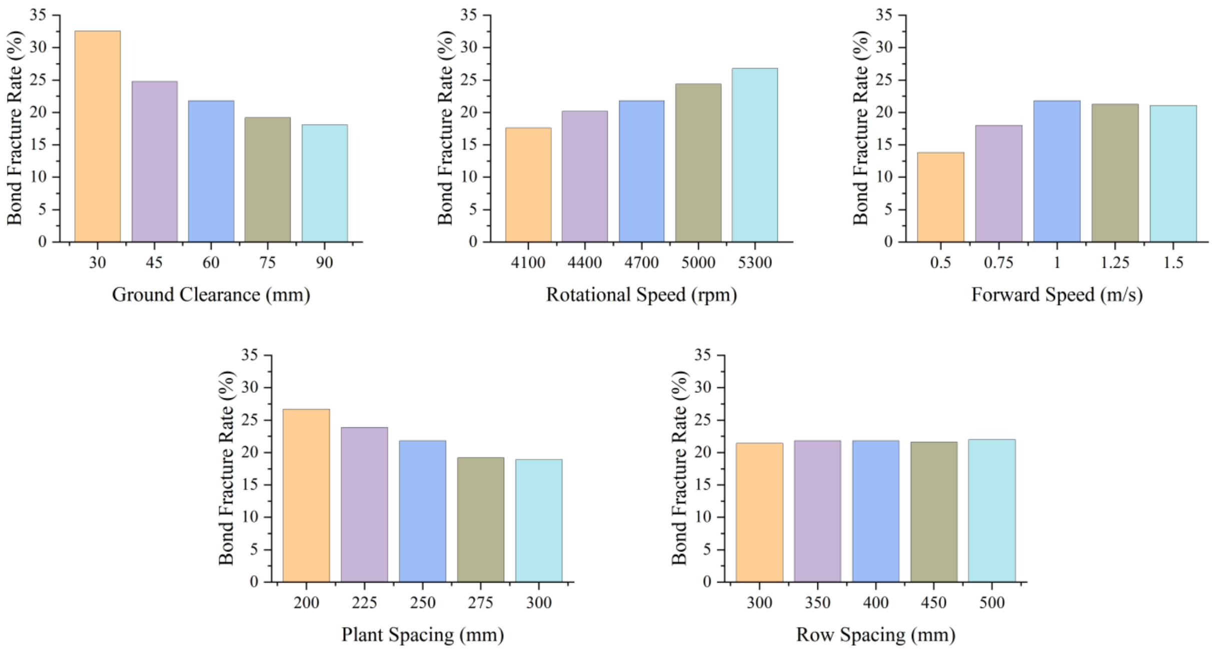

Fig. 7 - Effects of Operating Parameters on the Bond Fracture Rate

Increasing ground clearance from 30 to 90 mm reduced the bond fracture rate from 32.6% to 18.1% (44.5%), because higher clearance shifted flail action upward and reduced disturbance of the strongly bonded root-soil region.

Increasing rotor speed from 4100 to 5300 rpm raised the bond fracture rate from 17.6% to 26.8% (52.3%), as higher speed increased both impact energy and the number of impacts per unit travel distance.

Increasing forward speed from 0.5 to 1.5 m/s raised the bond fracture rate from 13.8% to 21.1%, although the change was only 0.7 percentage points between 1.0 and 1.5 m/s. Forward speed mainly affected the number of stubble contacts per unit time rather than the energy of individual impacts.

Increasing plant spacing from 200 to 300 mm reduced the bond fracture rate from 26.7% to 18.9% because fewer stubble units were encountered per unit area. Plant spacing is an inherent field condition rather than an adjustable machine parameter; therefore, it was evaluated only to characterize its influence on bond fracture rate and was not included in the selection of operating parameters.

Row spacing had the weakest effect: the bond fracture rate varied only from 21.4% to 22.0% over 300-500 mm, with no consistent monotonic trend.

The absolute variation associated with each factor is compared in Fig. 8.

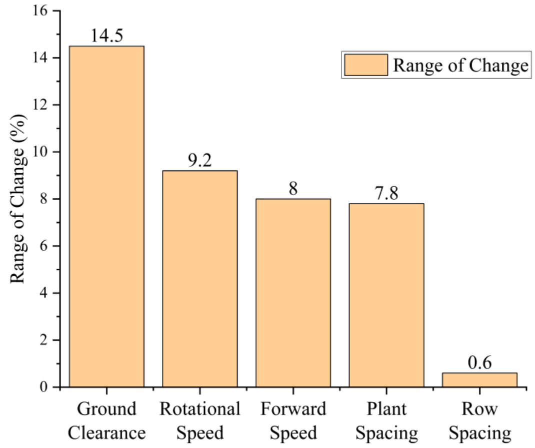

Fig. 8 - Comparison of Factors' Influence on Bond Fracture Rate

The influence order was ground clearance (14.5 percentage points) > rotor speed (9.2) > forward speed (8.0) > plant spacing (7.8) > row spacing (0.6). Thus, ground clearance and rotor speed were the principal controllable factors.

Based on the bond fracture trends within the tested parameter ranges, the candidate low-dust ranges were 60-75 mm for ground clearance, 4400-4700 rpm for rotor speed, and 0.75-1.0 m/s for forward speed. A condition of 75 mm ground clearance, 4400 rpm rotor speed, and 0.75 m/s forward speed was selected for subsequent combined DEM simulation and field comparison.

The observed effects of ground clearance and rotor speed are consistent with the general trend reported in previous agricultural-dust studies that stronger mechanical disturbance tends to increase particulate emissions. Significant differences in dust emissions have been reported among different tillage implements, with more intensive soil disturbance generally associated with higher particulate concentrations (*Çarman et al., 2023*). Agricultural tillage, planting, and harvesting operations have also been shown to generate measurable PM10 and PM2.5 emissions under field conditions (*Chen et al., 2017*). The present results extend these observations to a flail-type straw pickup header and further indicate that ground clearance and rotor speed are the principal controllable parameters governing mechanical particle detachment. The aerodynamic role of rotor speed is further examined through the CFD analysis in the following section.

Internal Flow Field of the Pickup Header and Analysis of Dust Sources

Steady MRF calculations were performed at 4100, 4700, and 5300 rpm to characterize the time-averaged internal flow field and its role in dust entrainment.

Velocity Field Distribution Characteristics

At 4700 rpm, the flow field was divided into four regions according to velocity magnitude and direction:

(1) High-speed rotation zone: airflow adjacent to the rotor formed a strong tangential shear layer, with typical velocities of 80-137 m/s and localized peaks of 153.3 m/s.

(2) Wall-guidance zone: airflow followed the curved inner housing wall at 30-60 m/s, supporting upward material transport.

(3) Inlet entrainment zone: negative pressure drew external air inward and upward through the lower opening at 5-18 m/s, providing the principal pathway for near-ground particle entrainment.

(4) Conveying-channel zone: downstream airflow was comparatively stable at 15-30 m/s and aligned with the channel axis.

The velocity distributions at the three rotor speeds are shown in Fig. 9.

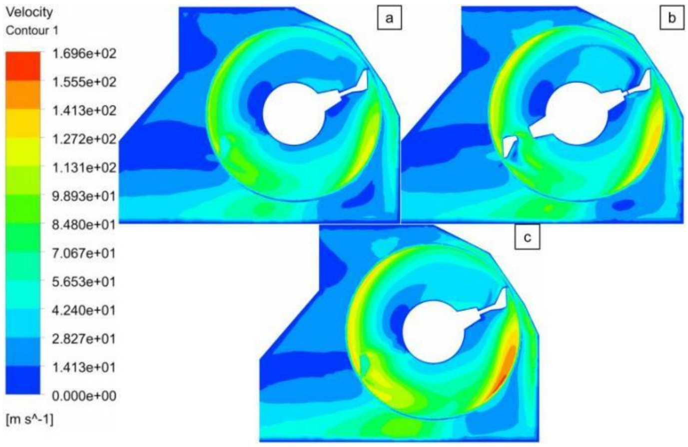

Fig. 9 - Velocity Contour Plot. (a) 4100 rpm; (b) 4700 rpm; (c) 5300 rpm

Increasing rotor speed raised velocities throughout the housing. For each 600 rpm increase, the upper velocity range in the high-speed zone increased by approximately 15-20 m/s, while the upper velocity in the inlet entrainment zone increased by about 4 m/s. The latter trend directly strengthened aerodynamic dust entrainment.

Mechanistic Interpretation of Dust Sources

Three dust-generation pathways were interpreted by relating the DEM detachment states to the corresponding CFD flow regions. Stubble-fragmentation dust originated from direct flail impact and was subsequently transported by the rotating airflow; root-extraction dust resulted from low-clearance disturbance of the root-soil interface followed by near-ground airflow entrainment; and airflow-entrainment dust consisted of loose surface particles lifted directly by the inlet flow. The first pathway increased with rotor speed, whereas the second was mainly associated with ground clearance.

Threshold-Based Comparison of Airflow Entrainment

The measured soil particle-size distribution and the calculated threshold velocities are shown in Fig. 10 and Table 6, respectively.

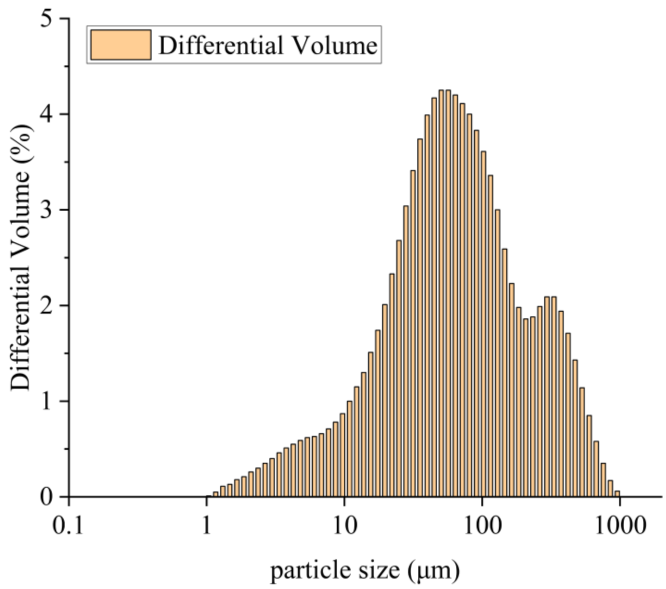

Fig. 10 - Particle Size Distribution

Table 6

Estimated threshold velocities for different particle size fractions

Particle Size (μm)	Equivalent Threshold Velocity (m/s)	Cumulative Volume Percentage (%)
10	0.89	9.38
50	1.99	48.95
100	2.81	68.70
200	3.97	83.72
300	4.87	89.68
500	6.29	96.85

Five monitoring points were placed on a horizontal plane 5 mm above the ground (Fig. 11). The upper inlet velocities of 12.7-16.1 m/s exceeded the recalculated equivalent mean-flow threshold velocities for all representative particle diameters up to 500 μm. Differences among rotor speeds therefore reflected the degree of threshold exceedance rather than whether entrainment occurred.

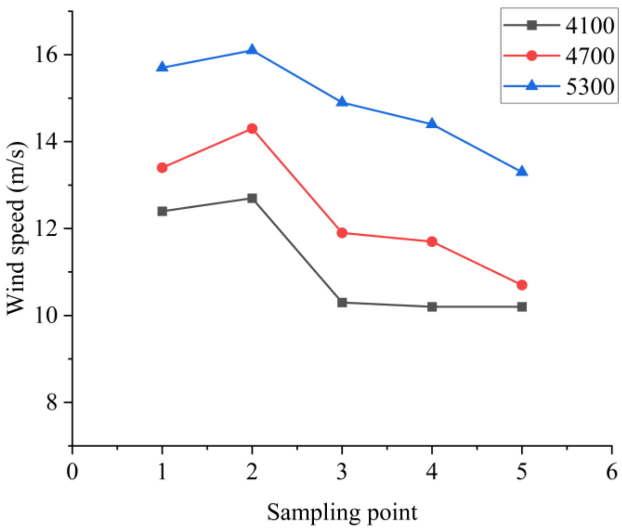

Fig. 11 - Wind Speed Comparison at Measuring Points

The threshold-exceedance ratios and bond fracture rates are compared in Table 7.

Table 7

Comprehensive comparison of airflow entrainment intensity and bond fracture rate at different rotor speeds

Rotor Speed (rpm)	Inlet Velocity Upper Limit (m/s)	Threshold-Exceedance Ratio U/U_t			Bond Fracture Rate (%)
		10-μm particle	50-μm particle	300-μm particle	
4100	12.7	14.3×	6.4×	2.6×	17.6
4700	14.3	16.1×	7.2×	2.9×	21.8
5300	16.1	18.1×	8.1×	3.3×	26.8

From 4100 to 5300 rpm, the velocity-to-threshold ratio increased by 26.8% for representative 10, 50, and 300 μm particles. Based on the calculation method described above, the estimated relative entrainment flux at 5300 rpm was approximately 2.04 times that at 4100 rpm.

Over the same speed range, the bond fracture rate increased by 52.3%. Rotor speed therefore produced a combined mechanical-aerodynamic effect: it increased the quantity of detached particles and simultaneously strengthened their entrainment. This mechanism predicts a larger change in measured dust concentration than in bond fracture rate alone and supports limiting rotor speed to 4400-4700 rpm.

Field Validation and Size-Resolved Particulate Concentrations

The background TSP concentration measured at the sampling point before operation was 56 μg/m³.

The combined DEM simulations yielded bond fracture rates of 34.6% for the dust-intensive condition and 19.1% for the selected low-dust condition, corresponding to a reduction of 44.8%. Field measurements showed the same trend: mean TSP concentration decreased from 3696.0 ± 515.6 to 1397.1 ± 229.2 μg/m3 (62.2%). The difference in TSP concentration between the two operating conditions was statistically significant according to a two-sided Welch's t-test ($t = 7.057$, $p = 0.0076$). The larger measured reduction relative to the bond fracture rate is consistent with simultaneous suppression of mechanical detachment and airflow entrainment.

The bond fracture rate should be interpreted as an indicator of the relative degree of particle detachment rather than as a direct predictor of airborne dust concentration. This index quantifies bond failure within the DEM model but does not account for particle size, the fraction of detached particles that actually becomes airborne, subsequent transport and deposition, re-entrainment of loose surface material, or ambient background particles. Therefore, the 44.8% reduction in bond fracture rate and the 62.2% reduction in measured TSP should not be expected to exhibit a one-to-one quantitative relationship. Their consistent trend supports the proposed mechanical-detachment mechanism, while the larger reduction in measured TSP is compatible with the simultaneous weakening of aerodynamic entrainment.

Size-fractionated measurements were used to determine whether the selected low-dust condition also reduced respirable and fine particulate concentrations.

Under the selected low-dust condition, PM_{10} and $PM_{2.5}$ accounted for 68.4% and 22.3% of TSP, respectively; under the dust-intensive condition, the corresponding proportions were 62.2% and 18.3% (Fig. 12).

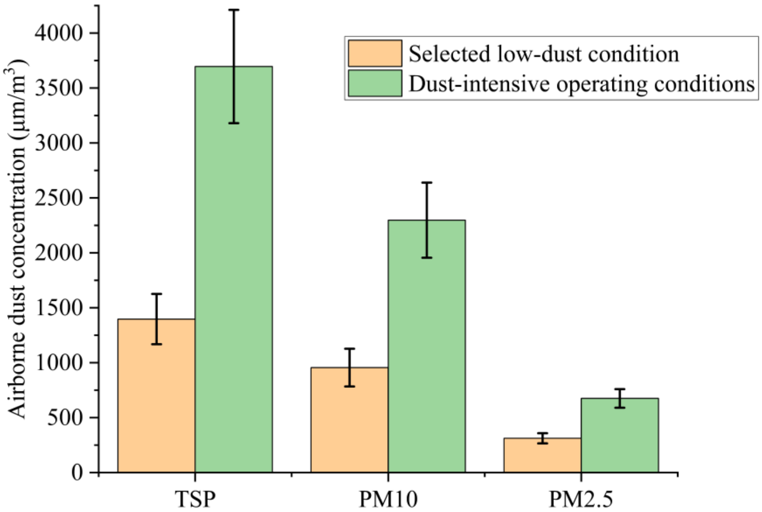

Fig. 12 - Particulate matter concentrations under different operating conditions.

Although the fine-particle proportions were slightly lower under the dust-intensive condition because coarse fragmentation debris increased, the absolute PM_{10} and $PM_{2.5}$ concentrations rose from 955.4 and 312.2 μg/m³ to 2297.4 and 675.2 μg/m³. The selected low-dust condition therefore reduced PM_{10} and $PM_{2.5}$ concentrations by 58.4% and 53.8%, respectively.

The measured TSP concentrations also provide useful context relative to previous harvesting studies. The TSP concentration of 1397.1 μg/m³ under the selected low-dust condition was slightly below the previously reported range of approximately 1500-3000 μg/m³ for harvesting operations, whereas the dust-intensive condition reached 3696.0 μg/m³ and exceeded this range (*Zhang et al., 2021; Xu et al., 2022a*). $PM_{2.5}$ accounted for 18.3%-22.3% of TSP in the present tests, which was lower than the 30%-45% proportion reported in previous harvesting studies (*Zhang et al., 2021; Xu et al., 2022a*). This difference may reflect variations in crop type, soil condition, machine structure, sampling position, and the relatively large contribution of coarse fragments generated by high-speed flail impact. Therefore, direct comparison of absolute concentrations among studies should be made cautiously.

These results demonstrate that parameter adjustment reduced both total and fine particulate emissions; however, the short sampling duration and fixed sampling location do not constitute a full occupational exposure assessment.

CONCLUSIONS

Ground clearance and rotor speed governed dust generation through different but interacting mechanisms. Ground clearance primarily affected mechanical particle detachment by changing the position of flail interaction relative to the strongly bonded root-soil region, whereas rotor speed influenced both impact-induced detachment and the strength of the inlet airflow. Relating the DEM particle-detachment characteristics to the CFD flow-field regions supported three mechanism-based dust-generation pathways: stubble fragmentation, root extraction, and direct airflow entrainment of loose surface particles.

Field measurements further showed that the selected combination of increased ground clearance and moderate rotor speed substantially reduced TSP, PM_{10}, and $PM_{2.5}$ concentrations relative to the dust-intensive condition, demonstrating the practical potential of operating-parameter adjustment for dust mitigation. The results also indicate that reducing excessive inlet negative pressure while maintaining pickup performance represents a promising direction for structural improvement.

Several limitations should be acknowledged. The DEM and CFD analyses were conducted independently rather than through fully coupled particle-flow simulation, and the bond fracture rate represents particle detachment rather than airborne dust concentration itself. Field validation was also limited to two operating conditions, a single field environment, three short-duration replicates per condition, and a fixed sampling position. Future studies should therefore examine a wider range of crops, soil conditions, and operating parameters; employ longer-duration and multi-point field measurements; investigate transient or coupled particle-airflow interactions; and evaluate pickup-header inlet modifications that reduce direct particle entrainment without compromising pickup efficiency.

ACKNOWLEDGEMENTS

This work was supported financially by the National Natural Science Foundation of China [52365035], the First-class Discipline Research Special Projects of the Inner Mongolia Autonomous Region [YLXKZX-NND-046], and the Natural Science Foundation of Inner Mongolia Autonomous Region [2025MS03015].

REFERENCES

[1] Aikins K. A., Ucgul M., Barr J. B., Jensen T. A., Antille D. L., Desbiolles J. M. A. (2021). Determination of discrete element model parameters for a cohesive soil and validation through narrow point opener performance analysis. *Soil and Tillage Research*, 213, 105123. https://doi.org/10.1016/J.STILL.2021.105123.

[2] Aikins K. A., Ucgul M., Barr J. B., Awuah E., Antille D. L., Jensen T. A., Desbiolles J. M. A. (2023). Review of discrete element method simulations of soil tillage and furrow opening. *Agriculture*, 13(3), 541. https://doi.org/10.3390/AGRICULTURE13030541.

[3] Chen G., Wang Q., Li H., He J., Lu C., Qin W., Mao L. (2024). Monitoring of farmland dust during tillage and sowing operations and comparative analysis of cultivation modes in the suburban areas of Beijing. *Soil & Tillage Research*, 237, 105991. https://doi.org/10.1016/J.STILL.2023.105991.

[4] Çarman K., Taner A., Mikailsoy F., Selvi K. Ç., Ungureanu N., Vlăduț N. V. (2023). Application of Computational Intelligence in Describing Dust Emissions in Different Soil Tillage Applications in Middle Anatolia. *Agriculture*, 13(5), 1011. https://doi.org/10.3390/agriculture13051011.

[5] Chen W., Tong D. Q., Zhang S., Zhang X., Zhao H. (2017). Local PM10 and PM2.5 emission inventories from agricultural tillage and harvest in northeastern China. Journal of Environmental Sciences, 57, 15–23. https://doi.org/10.1016/j.jes.2016.02.024.

[6] Cundall P. A., Strack O. D. L. (1980). A discrete numerical model for granular assemblies. *Géotechnique*, 30(3), 331–336. https://doi.org/10.1680/geot.1980.30.3.331.

[7] Du J., Heng Y., Zheng K., Luo C., Zhu Y., Zhang J., Xia J. (2022). Investigation of the burial and mixing performance of a rotary tiller using discrete element method. *Soil and Tillage Research*, 215, 105349. https://doi.org/10.1016/J.STILL.2022.105349.

[8] Foldager F. F., Munkholm L. J., Balling O., Serban R., Negrut D., Heck R., Green O. (2022). Modeling soil aggregate fracture using the discrete element method. *Soil and Tillage Research*, 218, 105295. https://doi.org/10.1016/J.STILL.2021.105295.

[9] Li R., Li H., Yang S., Lu C., Wu Z., Wang Z. (2025). DEM simulation of straw-soil-cutting system interactions for performance assessment of a spin-descent straw cutter. *Computers and Electronics in Agriculture*. https://doi.org/10.1016/J.COMPAG.2025.111022.

[10] Liang Z., Xu L., De Baerdemaeker J., Li Y., Saeys W. (2020). Optimisation of a multi-duct cleaning device for rice combine harvesters utilising CFD and experiments. *Biosystems Engineering*, 190, 25–40. https://doi.org/10.1016/j.biosystemseng.2019.11.016.

[11] Potyondy D. O., Cundall P. A. (2004). A bonded-particle model for rock. *International Journal of Rock Mechanics and Mining Sciences*, 41(8), 1329–1364. https://doi.org/10.1016/j.ijrmms.2004.09.011.

[12] Shao Y., Lu H. (2000). A simple expression for wind erosion threshold friction velocity. *Journal of Geophysical Research: Atmospheres*, 105(D17), 22437–22443. https://doi.org/10.1029/2000JD900304.

[13] Shih T. H., Liou W. W., Shabbir A., Yang Z., Zhu J. (1995). A new k-ε eddy viscosity model for high Reynolds number turbulent flows. *Computers and Fluids*, 24(3), 227–238. https://doi.org/10.1016/0045-7930(94)00032-T.

[14] Wang R., Li Q., Wang R., Chang C., Guo Z., Li J., Zhou N. (2021). Influence of wind velocity and soil size distribution on emitted dust size distribution: A wind tunnel study. *Journal of Geophysical Research: Atmospheres*, 126(7). https://doi.org/10.1029/2020JD033768.

[15] Wang R., Zhang Y., Zhang S., Li Q., Wang R., Li Z., Chang C., Guo Z., Zhou N. (2024). Comprehensive effect of soil particle size composition and wind speed on dust emission efficiency. *Journal of Geophysical Research: Atmospheres*, 129(3), e2023JD039618. https://doi.org/10.1029/2023JD039618.

[16] Wang X., Tian H., Xiao Z., Zhao K., Li D., Wang D. (2024). Numerical simulation and experimental study of corn straw grinding process based on computational fluid dynamics–discrete element method. *Agriculture*, 14(2), 325. https://doi.org/10.3390/agriculture14020325.

[17] Xu H., Zhang P., Hu Z., Mao E., You Z., Du Y. (2022). Analysis of dust emission characteristics of peanut whole-feed harvesting based on total amount collection method. *International Journal of Environmental Research and Public Health*, 19(23), 15937. https://doi.org/10.3390/IJERPH192315937.

[18] Xu H., Zhang P., Hu Z., Mao E., Yan J., Yang H. (2022). Analysis of dust diffusion from a self-propelled peanut combine using computational fluid dynamics. *Biosystems Engineering*, 215, 104–114. https://doi.org/10.1016/J.BIOSYSTEMSENG.2022.01.004.

[19] Xu H., Zhang P., Gu F., Hu Z., Yang H., Mao E., Du Y. (2023). Numerical simulation and experiment of dust suppression device of peanut whole-feed combine using computational fluid dynamics. *Agriculture*, 13(2), 329. https://doi.org/10.3390/AGRICULTURE13020329.

[20] Xu T., Gou Y., Huang D., Yu J., Li C., Wang J. (2024). Modeling and parameter selection of the corn straw-soil composite model based on the DEM. *Agriculture*, 14(11), 2075. https://doi.org/10.3390/AGRICULTURE14112075.

[21] Yang W., Li X., Zhang Y. (2022). Research progress and the development trend of the utilization of crop straw biomass resources in China. *Frontiers in Chemistry*, 10, 904660. https://doi.org/10.3389/FCHEM.2022.904660.

[22] Zhang P., Xu H., Hu Z., Chen Y., Cao M., Yu Z., Mao E. (2021). Characteristics of agricultural dust emissions from harvesting operations: Case study of a whole-feed peanut combine. *Agriculture*, 11(11), 1068. https://doi.org/10.3390/agriculture11111068.

[23] Zhang P., Xu H., Hu Z., Wang Q. (2023). Effects of agricultural machinery operations on PM2.5, PM10 and TSP in farmland under different tillage patterns. *Agriculture*, 13(5), 930. https://doi.org/10.3390/agriculture13050930.

[24] Zhao H., Huang Y., Liu Z., Liu W., Zheng Z. (2021). Applications of Discrete Element Method in the Research of Agricultural Machinery: A Review. *Agriculture*, 11(5), 425. https://doi.org/10.3390/AGRICULTURE11050425.

[25] Zhuo C., Tian H., Xiao Z., Mu Q., Tang L., Zhao K. (2025). Simulation analysis of mechanical response and failure mechanisms of maize stubble-soil composite based on discrete element method and fiber bundle model. *Computers and Electronics in Agriculture*, 236, 110452. https://doi.org/10.1016/J.COMPAG.2025.110452.